Normalized pulsed energy thresholding in a nonlinear optical loop mirror

M. A. Nahmias,* B. J. Shastri, A. N. Tait, M. Eder, Nicole Rafidi, Yue Tian, and P. R. Prucnal

Lightwave Communications Laboratory, Department of Electrical Engineering, Princeton University, Princeton, New Jersey 08544, USA

*Corresponding author: mnahmias@princeton.edu

Received 23 October 2014; revised 28 February 2015; accepted 2 March 2015; posted 5 March 2015 (Doc. ID 225348); published 8 April 2015

We demonstrate for the first time, to the best of our knowledge, that a Sagnac interferometer can threshold the energies of pulses. Pulses below a given threshold T are suppressed, while those above this threshold are normalized. The device contains an in-loop tunable isolator and 10.4 m of a highly doped silica fiber. We derive an analytical model of the nonlinear optical loop mirror's pulse energy transfer function and show that its energy transfer function approximates a step function for very high phase shifts ($>\pi$). We reveal some limitations of this approach, showing that a step-function transfer function necessarily results in pulse distortion in fast, nonresonant all-optical devices.

OCIS codes: (140.3490) Lasers, distributed-feedback; (060.2420) Fibers, polarization-maintaining; (060.3735) Fiber Bragg gratings; (060.2370) Fiber optics sensors.

http://dx.doi.org/10.1364/AO.54.003218

1. Introduction

All-optical signal processing has long been sought to circumvent the limitations of optoelectronic devices. One of the most critical nonlinear operations is thresholding: an ideal thresholder suppresses signals below some threshold Q_T and normalizes signals above Q_T. This differs from self-switching, in which pulses above Q_T need only be proportional to the input, as shown in Fig. 1(a). Optical self-switching has found use in many telecommunications applications—including the reduction of multiple access interference (MAI) in optical code division multiple access (OCDMA) [1–3] and 2R regeneration of pulses [4]. Nonetheless, normalized pulse energy thresholding has yet to be seriously investigated. Several unique applications could be enabled by a threshold response, including all-optical logic [5,6] and A/D conversion [7,8]. Asynchronous encoding schemes based on pulse position modulation (PPM) [9,10] could greatly benefit from a pulsed energy thresholder, which could be implemented as part of an optical computational primitive [11–13].

A variety of all-optical techniques have been proposed to enhance nonlinear effects for optical thresholding, including free carrier nonlinearities in semiconductor devices [14] and compact, high-Q resonators [15,16]. Recently, a microring-based device—a dual ring enhanced asymmetric demultiplexer (DREAM)—was proposed for both pulsed and continuous wave (CW) thresholding [17]. Although such resonator-based devices are compact, they are also wavelength-dependent and bandwidth-limited. Similarly, high-performance thresholding operations can be performed in the electronic domain [18], but electronics are severely bandwidth-limited by device and wire parasitics.

An alternative approach is the use of fiber nonlinearities, which are relatively wavelength-insensitive and limited in speed by only the Kerr effect (~fs). A nonlinear optical loop mirror (NOLM)

1559-128X/15/113218-07$15.00/0

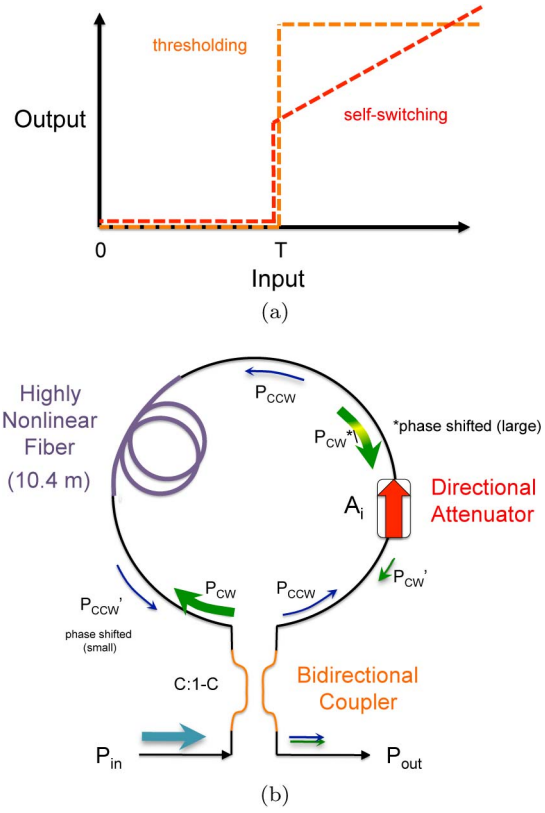

Fig. 1. (a) An ideal threshold function (orange). The input of a given variable is suppressed to 0 below a critical threshold Q_T, and normalized otherwise. This differs from self-switching, which contains a linear region above threshold (red). (b) Basic NOLM architecture. The two primary parameters of interest are the coupling ratio C of the bidirectional coupler and the attenuation A_i of the directional attenuator or tunable isolator. Two counterpropagating waves with unbalanced powers P_{ccw} and P_{cw} experience different phase shifts from the highly nonlinear fiber. The directional attenuator balances their powers at the output port when they recombine. The power-dependent phase shift results in an oscillating transfer function.

is a standard interferometric configuration which can contain a nonlinear fiber within the loop and exhibits an oscillating nonlinear power transfer function (PTF). Several recent proposals have added a directional attenuator (DA) within the ring interferometer, allowing for the powers of the counterpropagating pulses to be adjusted relative to one another [19–22]. Self-switching and continuous wave thresholding have been investigated in depth [22,23]. However, the NOLM's ability to normalize pulse energies above a threshold in addition to pulse suppression below threshold has yet to be demonstrated.

In this paper, we show for the first time, to the best of our knowledge, that this device can perform energy thresholding—both pulse suppression below threshold and pulse normalization above threshold—in theory and experiment. Although experimental results for this device were first shown in [22], the device was used in a low phase shift ($<\pi$) regime, so above-π effects (which include pulse normalization and shape distortion) were not considered. Here, we provide an analytical framework for pulse energies with known profiles, show that there is a flattening effect of the transfer function above a π phase shift, and extend these results to make general conclusions about pulse distortion in similar devices. First, we derive an energy transfer function (ETF) for stereotyped pulses that are commonly emitted by pulsed lasers. We show both theoretically and experimentally that it can simultaneously normalize pulses above threshold and suppress pulses below threshold. We also investigate and characterize pulse distortion within the context of energy thresholding in a more general case, which we show is unavoidable in fast, wavelength-insensitive devices.

2. Operational Principles

Below, we derive a pulse energy transfer function for the DA-NOLM. Although pulse power transfer functions have been measured experimentally [20,22], they lack a formal analytical framework. We begin with instantaneous power theory, previously derived in [19]. We neglect time-dependent effects such as dispersion in our model since the nonlinear fibers we utilize are fairly short (~m). We utilize the Kerr effect, which induces a change in the index of refraction $\Delta n = n_2 I$ for an input intensity I and nonlinear coefficient n_2 in the nonlinear fiber. For a NOLM with coupling ratio C ($0 \le C \le 1$) directional attenuation A_i, and nonlinear coefficient Γ (defined as $\Gamma = 2\pi L n_2/\lambda A_{\mathrm{eff}}$ for fiber length L and effective mode area A_{eff}) as shown in Fig. 1(b), we can write the instantaneous power transfer function in the following form:

$$P_{\mathrm{out}}(P_{\mathrm{in}}) = P_{\mathrm{in}}\left(\alpha + \beta - 2\sqrt{\alpha\beta}\,\cos(\phi_{\mathrm{CW}})\right), \qquad (1)$$

where $\alpha = A_i C^2$ and $\beta = (1-C)^2$ are the transmittances of the counterpropagating waves, $\Gamma_{\mathrm{eff}} = \Gamma(2C-1)$ is the effective nonlinear coefficient, and $\phi_{\mathrm{CW}} = \Gamma_{\mathrm{eff}} P_{\mathrm{in}}$ is the phase difference between counterpropagating pulses. Although Γ_{eff}, C, and A_i exhibit a wavelength dependence, this characteristic is much flatter than seen in resonant structures. In comparison, the NOLM is can be considered wavelength-insensitive.

Let us consider time-dependent pulsed inputs. For clarity, we formally redefine variables $\tilde{P}_{\mathrm{out}}(t)$ and $\tilde{P}_{\mathrm{in}}(t)$ as functions and relate them via a functional transformation $\tilde{P}_{\mathrm{out}} = \mathcal{F}[\tilde{P}_{\mathrm{in}}(t)]$. We assume input pulse profiles of the form $\tilde{P}_{\mathrm{in}}(t) = E_{\mathrm{in}}\Pi(t;\tau)$, where $\Pi(t;\tau)$ is a normalized pulse profile, E_{in} is the energy of the pulse, and τ the pulse width. Noting that $E_{\mathrm{out}}(E_{\mathrm{in}}) = \int_{-\infty}^{\infty} \tilde{P}_{\mathrm{out}}(t)\mathrm{d}t$, we can derive a pulse energy function of the form

$$E_{\mathrm{out}}(E_{\mathrm{in}}) = E_{\mathrm{in}}\left[\alpha + \beta - 2\sqrt{\alpha\beta}\,\Theta(E_{\mathrm{in}})\right], \qquad (2)$$

where α, β are the same as before, and

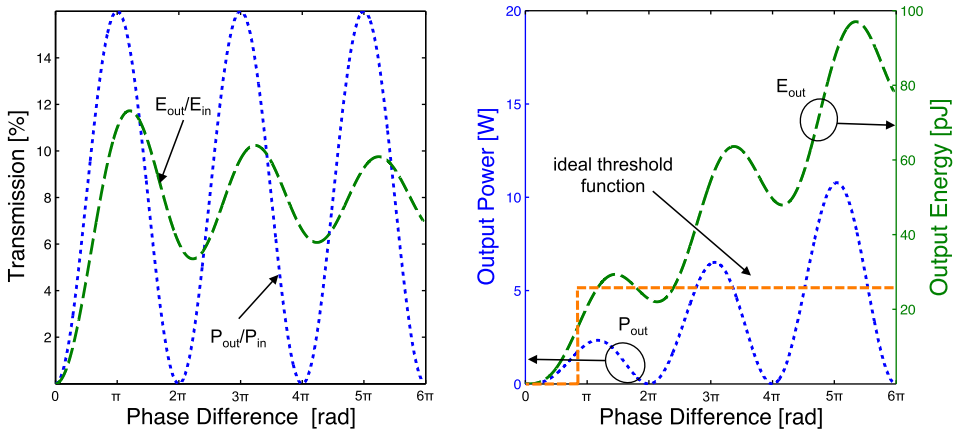

Fig. 2. Transfer function simulations of a NOLM with $C = .8$ and $A_i = 1/16$. (a) Transmission functions for both instantaneous power (blue dotted) and hyperbolic secant pulse energy (green dashed) as a function of the phase differences $\phi_{\mathrm{CW}} = \Gamma_{J\mathrm{eff}} P_{\mathrm{in}}$ and $\phi_P = \Gamma_{\mathrm{eff}} E_{\mathrm{in}}/2\tau$, respectively, of the waves on the output port. The phase difference is linearly proportional to the input power and energy and is used as a basis for cross-comparison. Curves were computed using Eqs. (1), (3), and (4). Since pulses contain a distribution of powers, the oscillating transmission function becomes softer and flatter. The degree to which this occurs depends on how close the shapes of input pulses are to square-like profiles. (b) Power and energy transfer functions as a function of the phase differences $\phi_{CW} = \Gamma P_{\mathrm{in}}$ and $\phi_P = \Gamma_{\mathrm{eff}} E_{\mathrm{in}}/2\tau$, where we have assumed $\Gamma = .525$, and a sech pulse with width of $\tau = 7$ ps. A step function (orange dotted) with threshold P_T is shown for comparison. The energy transfer function resembles a step function between phases 0 and 2.5π.

$$\Theta(E_{\mathrm{in}}) = \int_{-\infty}^{\infty} \Pi(t;\tau)\cos(\Gamma_{\mathrm{eff}} E_{\mathrm{in}} \Pi(t;\tau))\mathrm{d}t. \qquad (3)$$

This quantity has a very strong dependence on the pulse shape $\Pi(t;\tau)$. The special case of an idealized rectangular pulse of the form $\Pi(t;\tau) = \frac{1}{\tau}\mathrm{rect}(t/\tau)$ with pulse width τ results in the function $\Theta(E_{\mathrm{in}})$ reducing to $\cos[(\Gamma_{\mathrm{eff}}/\tau)E_{\mathrm{in}}]$—the ETF and PTF [Eq. (1)] become analogous.

A more realistic model for ultrashort pulses are squared hyperbolic secant functions, which have normalized pulse profiles of the form $\Pi(t;\tau) = \frac{1}{2\tau}\mathrm{sech}^2(t/\tau)$ and commonly model fundamental solitons, pulses from mode-locked lasers, and high-powered pulses from Q-switched lasers [24]. For convenience, let us define the *peak phase* $\phi_P = \Gamma_{\mathrm{eff}} E_{\mathrm{in}}/2\tau$, the phase difference between modes at the *peak powers* of incident pulses. Then, the value of $\Theta(\phi_P)$ can be computed through Eq. (3):

$$\Theta(\phi_P) = \sqrt{\frac{\pi}{2\phi_P}}\left[\cos(\phi_P)\cdot C\left(\sqrt{\frac{2\phi_P}{\pi}}\right) + \sin(\phi_P)\cdot S\left(\sqrt{\frac{2\phi_P}{\pi}}\right)\right], \qquad (4)$$

where $C(x)$ and $S(x)$ are Fresnel integrals.

Figure 2 illustrates a comparison between the instantaneous power model and the sech pulse energy models, plotted as function of their phase differences ϕ and ϕ_P. We define a pulse threshold P_T, on the boundary of pulse suppression/normalization, which occurs at the first inflection point in Eq. (2). Transmission curves (left) and transfer functions (right) are shown using an simulated DA-NOLM. For low values, the energy transfer function increases rapidly until it reaches a π phase shift, where it begins to decrease and levels off. This fairly small region closely resembles a *step function*, which is the desired characteristic of a thresholder. Although the region between the zero and one levels is fairly linear, the device still meets the minimal requirements for robust optical pulse processing: it contains attractive fixed points at the zero and one level regions, and a repulsive fixed point at the threshold E_T.

3. Pulsed Thresholding

We sent in a stream of pulses with various energies using part of the experimental configuration illustrated in Fig. 3. Pulses of 7 ps were generated by a mode-locked laser (MLL) at a 10 GHz repetition

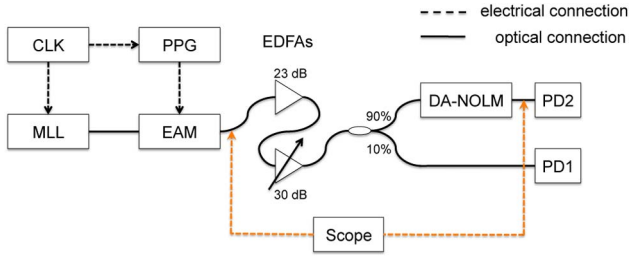

Fig. 3. Experimental setup used to measure pulses and PTFs. MLL, mode-locked laser; CLK, clock; PPG, pulse pattern generator; EAM, electro-absorption modulator; EDFA, erbium-doped fiber amplifier; DA-NOLM, thresholder; PD1, first (output) photodetector; PD2, second (input) photodetector. The pulse window in Fig. 4 was measured using the scope at the output of the EAM and the DA-NOLM. Power sweeps were measured using PD1 and PD2 while tuning the 30 dB EDFA.

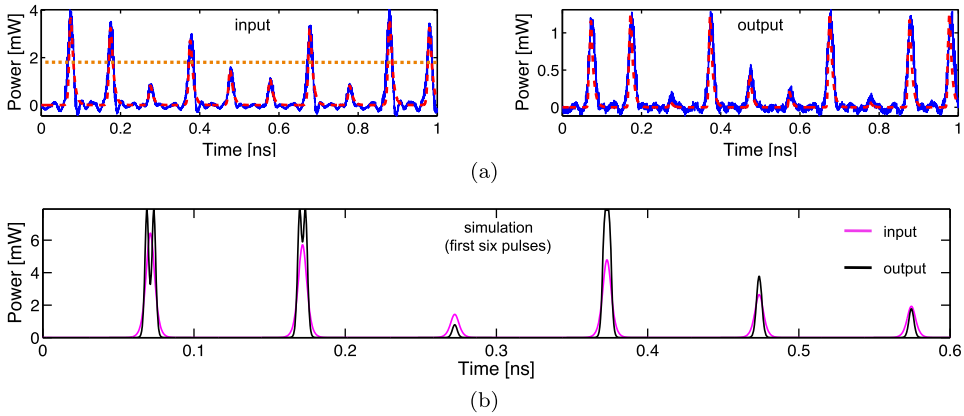

Fig. 4. (a) Pulses measured (blue) and modeled (red) at the input and output of the DA-NOLM. The device simultaneously normalizes and suppresses pulses above and below threshold, respectively. The model based on Eq. (2) includes low-pass filtering to account for scope sampling resolution. This model closely predicts what is measured experimentally. The orange, dotted line represents the input threshold P_T of the NOLM. (b) The same model, but without low-pass filtering both at the input (purple) and output (black) for the first six pulses in (a). The model is successful in producing experimentally valid results, but also provides further insights beyond what is visible with experiment.

rate. The pulse train was then modulated by an electro-absorption modulator (EAM) driven by a pulse pattern generator (PPG). EAM biasing allowed for the variety of input pulse energies shown in Fig. 4 for every 8-pulse window. The resulting signal traveled through cascaded erbium-doped fiber amplifiers (EDFAs), which boosted the signal to approximately 30 dBm to enhance nonlinear phase shifts as they traveled through the NOLM. The device itself was built in a similar fashion to the one described in [22]: it included 10.4 m of nonholey silica fiber as a nonlinear element, a tunable isolator that acted as a variable DA, an intraloop polarization controller, and a tunable coupler.

To confirm that our experimental results were consistent with our theoretical model, we simulated the experiment in a computational environment. Pulses of various energies were modeled using typical hyperbolic secant pulse shapes with different peak powers P_p. The NOLM-DA acted upon the pulses instantaneously via Eq. (1). A simple low-pass filter (LPF) was included to model the sampling resolution of the scope.

Results are shown in Fig. 4. Higher energy pulses were normalized to the same amplitude, whereas lower energy pulses were suppressed toward a zero-amplitude attractor. There was also a strong agreement between the pulse profiles seen in the experiment (blue) and those modeled (red) as seen in Fig. 4(a).

One key property revealed by modeling is that the scope is unable to capture the distortion of the pulses as they travel through the NOLM, shown in Fig. 4(b). This distortion is a natural consequence of the very properties that make the NOLM advantageous: it acts nearly instantaneously and has a transfer function—Eq. (1)—that is nonmonotonic. As a result, this effect is difficult to avoid in any device that utilizes phase interference. One solution to smooth out the pulse is putting a bandpass filter (BPF) on the output port [25], but doing so results in strong frequency dependence, offsetting one of the device's key advantages.

4. Measurements of Energy Transfer Functions

Transfer function measurements were performed using a setup illustrated in Fig. 3. A 90/10 coupler diverted 10% of the input power for power monitoring to a photodetector (PD1), while the remaining 90% traveled into the device. We chose an uneven coupling ratio to maintain large input powers. Output pulses were incident on a second photodetector (PD2). Both detectors measured the average powers P_{avg} of the input and output signals. Modulation of the tunable EDFA depicted in Fig. 3 allowed for control over the energies of the incoming pulses.

Our results (Fig. 5) show a strong agreement between experimental and theoretical measurements. The measured average power gives us insight into the shape of the energy transfer function, since the average power is linearly proportional to the pulse energy. Although there is some divergence between the theoretical models and experimental measurements for very large phase shifts ($\phi_d > 2\pi$)—which may be a result of pulse distortion from EDFA saturation—we nonetheless observed consistent results for our range of interest ($0 < \phi_d < 2\pi$).

5. Pulse Distortion

It was shown in Section 3 that the NOLM's unique properties also lead to pulse distortion over large ($>\pi$) phase shifts. As we show here, pulse distortion is inherent in all interferometric devices that perform step function thresholding on nonrectangular pulses, and arises from the device's fast reaction time (<1 ps) in comparison to input signals.

Let us assume our device acts instantaneously on input powers, and is not dependent on any other

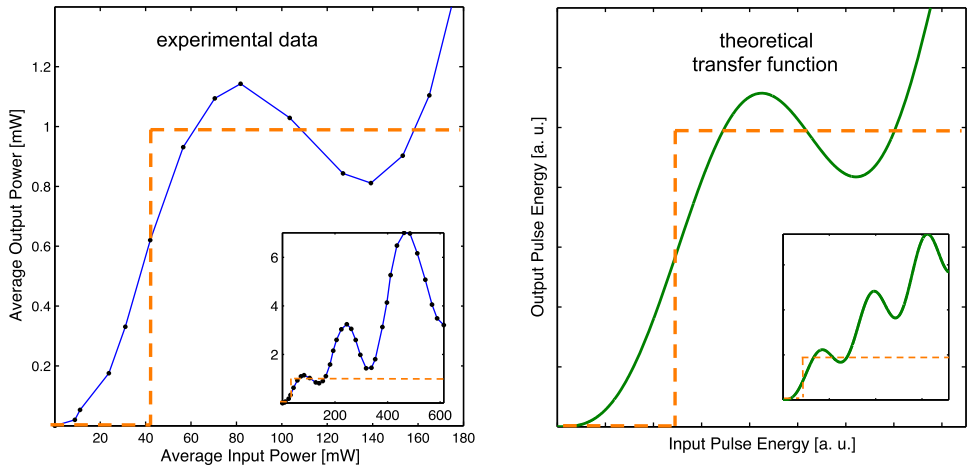

(a) (b)

Fig. 5. (a) An experimental transfer function of input and output powers compared to (b) the theoretically predicted energy transfer function in Eq. (2) for pulsed inputs. This plot reveals the source of pulse normalization, the flat region above a π phase shift. The experimental sweep was obtained using techniques described in Section 4—dots represent data points.

property of the incoming wave. This assumption is valid if input signals are approximated as slowly varying, a condition which is met for interferometers with equal path lengths. Suppose we wanted to create a perfect pulse energy thresholder, or a device with a transfer function of the form $E^*_{\text{out}}(E_{\text{in}}) \equiv E_N \text{H}(E_{\text{in}} - E_T)$, where $\text{H}(x)$ is the Heaviside step function, E_N is the normalized pulse energy above threshold, and E_T is the threshold itself. The relationship between the instantaneous PTF $P_{\text{out}}(P_{\text{in}})$ and ideal energy transfer function (ETF) $E_{\text{out}}(E_{\text{in}})$ can be viewed as a *functional transformation* $\Omega{:}\mathbb{P} \to \mathbb{E}$ from the power to energy domains. We can define a transformation between the power and energy transfer functions for an arbitrary pulse shape $\Pi(t;\tau)$:

$$f(E_{\text{in}}) = \Omega[g(P_{\text{in}})] = \int_{-\infty}^{\infty} g(E_{\text{in}}\Pi(t;\tau))\text{d}t. \tag{5}$$

The existence of Ω implies that there is a *reverse* transformation $g(P_{\text{in}}) = \Omega^{-1}[f(E_{\text{in}})]$. This is easy to compute for the case of a rectangular pulse profile $\Pi(t;\tau) = \frac{1}{\tau}\text{rect}(t/\tau)$—i.e., $\Omega[g(P_{\text{in}})] = \tau g(E_{\text{in}}/\tau)$ and $\Omega^{-1}[g(E_{\text{in}})] = \frac{1}{\tau} f(\tau P_{\text{in}})$. In the general case, the instantaneous PTF of an ideal thresholder can be expressed in the following form:

$$P^*_{\text{out}}(P_{\text{in}}) = \Omega^{-1}[E_N \text{H}(E_{\text{in}} - E_T)]. \tag{6}$$

For our simulation, we assumed that our pulse has a sech profile s.t. $\Pi(t;\tau) = \frac{1}{2\tau}\text{sech}^2(t/\tau)$ and calculated the inverse transform Ω^{-1} of a perfect thresholder via

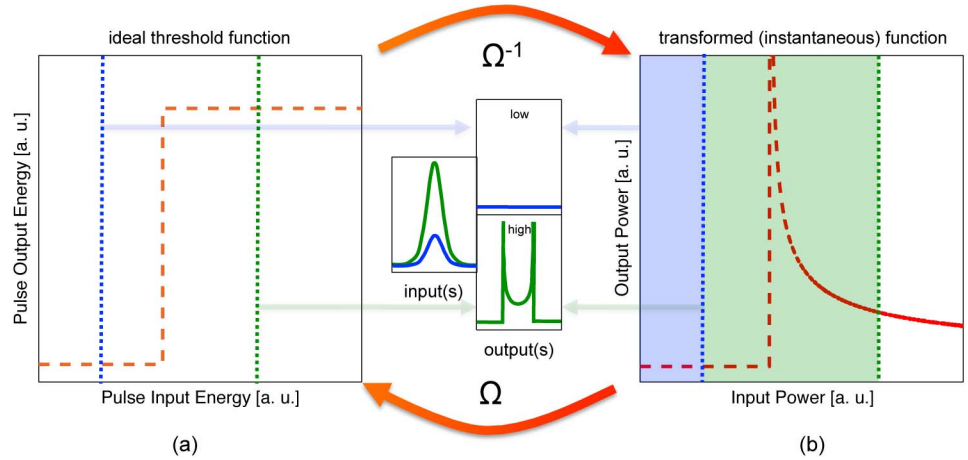

(a) (b)

Fig. 6. $\Omega{:}\mathbb{P} \to \mathbb{E}$ transformation between the energy and power domains for an ideal thresholer, assuming instantaneity and wavelength independence. (a) An ideal step function for pulse energies. Input pulse energies for output pulse profiles (middle) are shown with the blue and green dotted lines, below and above threshold, respectively. (b) The instantaneous function needed for a perfect pulse energy thresholder. Since the function is nonmonotonic, pulses will distort and bifurcate above threshold (middle). Shaded are the input power range for a pulse below (blue) and above (green) threshold.

a gradient descent search algorithm. The result is shown in Fig. 6. The computed instantaneous function [Fig. 6(b)] contains a sharp asymptotic jump followed by a falling tail. The output pulses above threshold, as a result, are highly distorted.

Although our simulation focused on hyperbolic secant pulses, the results here can be generalized: once the peak power of any given pulse hits the power threshold P_T, the instantaneous function must spike to extremely high values to create a pulse with the correct one-level energy. Likewise, a falling tail is necessary to keep the energy normalized for increasing input energies. The resulting nonmonotonic function will lead to bifurcated pulses as shown in Fig. 6. Thus, pulse distortion is inescapable for energy thresholding in a general class of fast, interferometric devices. There is a fundamental trade-off between threshold shape and pulse distortion that cannot be avoided without losing instantaneity.

6. Discussion

Although the NOLM-DA meets the minimum requirements for pulse energy thresholding, its transfer function still deviates from a perfect step function. Relative to resonant-based or filtered approaches (cite DREAM, Nicole), the NOLM exhibits a reduced extinction ratio between the zero and one levels (~13 dB), pulse distortion above threshold, and a low dynamic range (full operating range two times the threshold P_T). It may have limited applicability for particularly noisy or sensitive systems. In order to improve the transfer function characteristic while preserving the properties of this device which are advantageous—including wavelength insensitivity and an extremely fast (~fs) response time—one possible solution is to cascade several NOLM devices in sequence, in order to enhance the sharpness of the thresholding transfer function. Nonetheless, without careful loss management, an amplifier may be needed in between each NOLM, which could offset the advantages of the device. Further improvements to the thresholding characteristic through alternative or cascaded loop architectures remains an open topic of exploration.

7. Conclusions

We have presented a model of optical pulse thresholding in a NOLM and have experimentally verified its predictions, showing for the first time, to the best of our knowledge, simultaneous pulse suppression and normalization below and above a given threshold, respectively, in a terahertz bandwidth, wavelength-insensitive device. The presented pulsed theory builds on the previous instantaneous theory, and provides a framework for pulsed-based energy discrimination. We find that pulse shape distortion can have a significant effect on the energy transfer function, making the pulsed theory considerably more accurate at predicting experimental measurements. We have also shown that step-function-like thresholding of pulse energies necessarily results in pulse distortion for a general class of interferometric devices that exhibit instantaneity. The NOLM is one of the simplest fiber circuits for all-optical energy discrimination based on self-phase modulation. Step function energy thresholding in the NOLM—owing to its unique properties—could find use in a number of high-performance optical signal processing applications, including noise suppression in pulsed-based amplitude-shift keying, all-optical A/D conversion, soliton logic, and photonic spike processing.

The authors wish to thank Mable Fok for her valuable suggestions regarding the experimental setup and insightful discussions.

References

1. J. Lee, P. Teh, Z. Yusoff, M. Ibsen, W. Belardi, T. M. Monro, and D. J. Richardson, "A holey fiber-based nonlinear thresholding device for optical CDMA receiver performance enhancement," IEEE Photon. Technol. Lett. **14**, 876–878 (2002).
2. P. R. Prucnal, *Optical Code Division Multiple Access: Fundamentals and Applications* (CRC Press, 2005).
3. J. Penon, Z. A. El-Sahn, L. A. Rusch, and S. LaRochelle, "Spectral-amplitude-coded OCDMA optimized for a realistic FBG frequency response," J. Lightwave Technol. **25**, 1256–1263 (2007).
4. F. Seguineau, B. Lavigne, D. Rouvillain, P. Brindel, L. Pierre, and O. Leclerc, "Experimental demonstration of simple NOLM-based 2R regenerator for 42.66 Gbit/s WDM long-haul transmissions," in *Optical Fiber Communication Conference* (IEEE, 2004).
5. S. Ma, Z. Chen, H. Sun, and N. K. Dutta, "High speed all optical logic gates based on quantum dot semiconductor optical amplifiers," Opt. Express **18**, 6417–6422 (2010).
6. F. Ramos, E. Kehayas, J. M. Martinez, R. Clavero, J. Marti, L. Stampoulidis, D. Tsiokos, H. Avramopoulos, J. Zhang, P. V. Holm-Nielsen, N. Chi, P. Jeppesen, N. Yan, I. Tafur, Monroy, A. M. J. Koonen, M. T. Hill, Y. Liu, H. J. S. Dorren, R. Van Caenegem, D. Colle, M. Pickavet, and B. Riposati, "IST-LASAGNE: towards all-optical label swapping employing optical logic gates and optical flip-flops," J. Lightwave Technol. **23**, 2993–3011 (2005).
7. Y. Miyoshi, S. Takagi, S. Namiki, and K.-I. Kitayama, "Multi-period PM-NOLM with dynamic counter-propagating effects compensation for 5-bit all-optical analog-to-digital conversion and its performance evaluations," J. Lightwave Technol. **28**, 415–422 (2010).
8. R. Pant, C. Xiong, S. Madden, B. L. Davies, and B. J. Eggleton, "Investigation of all-optical analog-to-digital quantization using a chalcogenide waveguide: a step towards on-chip analog-to-digital conversion," Opt. Commun. **283**, 2258–2262 (2010).
9. B. J. Shastri, M. A. Nahmias, A. N. Tait, Y. Tian, B. Wu, and P. R. Prucnal, "Graphene excitable laser for photonic spike processing," in *Proceedings of the IEEE Photonics Conference (IPC)*, Seattle, WA, 2013, pp. 1–3.
10. M. A. Nahmias, A. N. Tait, B. J. Shastri, and P. R. Prucnal, "An evanescent hybrid silicon laser neuron," in *Proceedings of the IEEE Photonics Conference (IPC)*, Seattle, WA, 2013, pp. 93–94.
11. M. A. Nahmias, B. J. Shastri, A. N. Tait, and P. R. Prucnal, "A leaky integrate-and-fire laser neuron for ultrafast cognitive computing," IEEE J. Sel. Top. Quantum Electron. **19**, 1800212 (2013).
12. A. N. Tait, M. A. Nahmias, Y. Tian, B. J. Shastri, and P. R. Prucnal, "Photonic neuromorphic signal processing and computing," in *Nanophotonic Information Physics* (Springer, 2014), pp. 183–222.
13. A. N. Tait, M. A. Nahmias, B. J. Shastri, and P. R. Prucnal, "Broadcast and weight: an integrated network for scalable photonic spike processing," J. Lightwave Technol. **32**, 3427–3439 (2014).

14. K.-L. Deng, I. Glesk, K. Kang, and P. Prucnal, "Unbalanced TOAD for optical data and clock separation in self-clocked transparent OTDM networks," IEEE Photon. Technol. Lett. **9**, 830–832 (1997).
15. V. Van, T. Ibrahim, K. Ritter, P. Absil, F. Johnson, R. Grover, J. Goldhar, and P.-T. Ho, "All-optical nonlinear switching in GaAs-AlGaAs microring resonators," IEEE Photon. Technol. Lett. **14**, 74–76 (2002).
16. T. Tanabe, M. Notomi, S. Mitsugi, A. Shinya, and E. Kuramochi, "All-optical switches on a silicon chip realized using photonic crystal nanocavities," Appl. Phys. Lett. **87**, 151112 (2005).
17. A. N. Tait, B. J. Shastri, M. P. Fok, M. A. Nahmias, and P. R. Prucnal, "The DREAM: an integrated photonic thresholder," J. Lightwave Technol. **31**, 1263–1272 (2013).
18. Y. Ehrlichman, O. Amrani, and S. Ruschin, "Integrated photonic threshold comparator based on square-wave synthesis," Opt. Express **21**, 14251–14261 (2013).
19. A. G. Striegler, M. Meissner, K. Cvecek, K. Sponsel, G. Leuchs, and B. Schmauss, "NOLM-based RZ-DPSK signal regeneration," IEEE Photon. Technol. Lett. **17**, 639–641 (2005).
20. O. Pottiez, E. Kuzin, B. Ibarra-Escamilla, J. Camas-Anzueto, and F. Gutierrez-Zainos, "Experimental demonstration of NOLM switching based on nonlinear polarisation rotation," Electron. Lett. **40**, 892–894 (2004).
21. O. Pottiez, E. Kuzin, B. Ibarra-Escamilla, J. Camas-Anzueto, and F. Gutiérrez-Zainos, "Easily tunable nonlinear optical loop mirror based on polarization asymmetry," Opt. Express **12**, 3878–3887 (2004).
22. K. Kravtsov, P. R. Prucnal, and M. M. Bubnov, "Simple nonlinear interferometer-based all-optical thresholder and its applications for optical CDMA," Opt. Express **15**, 13114–13122 (2007).
23. W. S. Wong, S. Namiki, M. Margalit, H. A. Haus, and E. P. Ippen, "Self-switching of optical pulses in dispersion-imbalanced nonlinear loop mirrors," Opt. Lett. **22**, 1150–1152 (1997).
24. A. E. Siegman, *Lasers* (University Science Books, 1986).
25. N. S. Rafidi, K. S. Kravtsov, Y. Tian, M. P. Fok, M. A. Nahmias, A. N. Tait, and P. R. Prucnal, "Power transfer function tailoring in a highly Ge-doped nonlinear interferometer-based all-optical thresholder using offset-spectral filtering," IEEE Photon. J. **4**, 528–534 (2012).